UC Davis
UC Davis Previously Published Works

Title

Vapor-Wall Deposition in Chambers: Theoretical Considerations

Permalink

Authors

McVay, Renee C
Cappa, Christopher D
Seinfeld, John H

Publication Date

DOI

Peer reviewed

Vapor Wall Deposition in Chambers: Theoretical Considerations

Renee C. McVay,[†] Christopher D. Cappa,[‡] and John H. Seinfeld[*,†,¶]

Division of Chemistry and Chemical Engineering, California Institute of Technology, Pasadena, CA 91125, Department of Civil and Environmental Engineering, University of California at Davis, Davis, CA 95616, and Division of Engineering and Applied Science, California Institute of Technology, Pasadena, California 91125, United States

E-mail: seinfeld@caltech.edu

Phone: (626) 395-4635. Fax: (626) 796-2591

Abstract

In order to constrain the effects of vapor wall deposition on measured secondary organic aerosol (SOA) yields in laboratory chambers, Zhang et al. (2014) varied the seed aerosol surface area in toluene oxidation and observed a clear increase in the SOA yield with increasing seed surface area. Using a coupled vapor-particle dynamics model, we examine the extent to which this increase is the result of vapor wall deposition versus kinetic limitations arising from imperfect accommodation of organic species into the particle phase. We show that a seed surface area dependence of the SOA yield is present only when condensation of vapors onto particles is kinetically limited. The existence of kinetic limitation can be predicted by comparing the characteristic timescales of gas-phase reaction, vapor wall deposition, and gas-particle

---

[*]To whom correspondence should be addressed
[†]Division of Chemistry and Chemical Engineering, California Institute of Technology, Pasadena, CA 91125
[‡]Department of Civil and Environmental Engineering, University of California at Davis, Davis, CA 95616
[¶]Division of Engineering and Applied Science, California Institute of Technology, Pasadena, California 91125, United States

equilibration. The gas-particle equilibration timescale depends on the gas-particle accommodation coefficient α_p. Regardless of the extent of kinetic limitation, vapor wall deposition depresses the SOA yield from that in its absence since vapor molecules that might otherwise condense on particles deposit on the walls. To accurately extrapolate chamber-derived yields to atmospheric conditions, both vapor wall deposition and kinetic limitations must be taken into account.
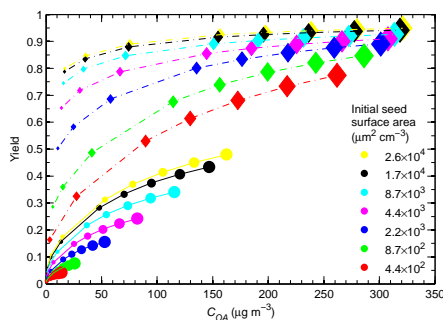
Introduction

The formation of secondary organic aerosol (SOA) is represented in atmospheric models by SOA yields (mass of SOA formed per mass of parent volatile organic compound (VOC) reacted), which are determined in laboratory chambers. It has been established that current atmospheric models using chamber-derived yields significantly underpredict ambient SOA levels (*1–7*). Recent work has suggested that experimentally-determined SOA yields could be systematically biased low due to wall deposition of organic vapors that would otherwise contribute to SOA growth (*8–10*).

Zhang et al. (*11*) report the results of chamber studies aimed to constrain experimentally the effect of vapor wall deposition on SOA yields. In these experiments, involving toluene as the parent VOC, the level of seed aerosol was systematically varied in order to modulate the competition between growing particles and the chamber walls for condensable vapors. The statistical oxidation model (SOM) of Cappa et al. (*12, 13*), updated to account for dynamic partitioning between

2

vapors and particles and vapors and the chamber walls, was fit to the data. The results demonstrate clear experimental evidence of the role of vapor wall deposition on measured SOA yield. The present work analyzes theoretically the observed dependence of SOA yields on seed surface area by simulating the key elements of VOC oxidation and aerosol chamber dynamics. The representation of gas-phase VOC oxidation chemistry in such an analysis need not be complex, as the essential factors are the rate of progressive oxidation and the volatilities of the oxidation products. The present study is intended to provide a theoretical structure for assessing the effects of key processes on vapor wall deposition in laboratory chamber studies of SOA formation.

Methods

Gas-Phase VOC Oxidation

To evaluate theoretically the effect of vapor wall deposition in a typical chamber experiment, the gas-phase chemistry need only represent the progressive oxidation of a parent VOC. We consider oxidation of a parent VOC, species A, occurring sequentially according to A→B→C→D. Species A represents the completely volatile parent VOC, and species B through D are oxidation products, with mass saturation concentrations decreasing by one order of magnitude per each generation of reaction. Each oxidation step can be considered to represent reaction with OH, although the chemical details are not required. With no loss of generality, each species in this idealized mechanism is assigned the same molecular weight (200 g mol^{-1}); in so doing, the maximum SOA yield possible is 1.0. Since oxidation leads to progressively lower volatility species, the maximum yield will always be reached at sufficiently long time if there are no additional vapor loss mechanisms, such as wall deposition.

Aerosol Dynamic Model

We have developed a coupled vapor-particle dynamics model following the framework of the Aerosol Parameter Estimation (APE) model of Pierce et al. (*14*). The model simulates coagulation, condensation/evaporation, and particle and vapor wall deposition in a well-mixed laboratory chamber in which a VOC is being oxidized to SOA. The SOA yield is determined as the ratio of the total mass of organic oxidation products condensed on both suspended and wall-deposited particles to the total mass of VOC reacted (both expressed in units of μg m^{-3}).

The aerosol size distribution is represented using fixed size bins, with specified mean diameters, so that the evolution of the chamber aerosol is reflected by the time variation of the particle number concentration in each bin. The aerosol general dynamic equation is expressed in terms of the particle size distribution function $n(D_p,t)$ as

$$\left(\frac{\partial n(D_p,t)}{\partial t}\right) = \left(\frac{\partial n(D_p,t)}{\partial t}\right)_{coag} + \left(\frac{\partial n(D_p,t)}{\partial t}\right)_{cond/evap} + \left(\frac{\partial n(D_p,t)}{\partial t}\right)_{wall\ loss} \tag{1}$$

where D_p is the particle diameter.

The equation governing the change in the number distribution due to coagulation is (*14*, *15*)

$$\left(\frac{\partial n(D_p,t)}{\partial t}\right)_{coag} = \frac{1}{2}\int_0^{D_p} K((D_p^3 - q^3)^{1/3},q)n((D_p^3)^{1/3},t)n(q,t)dq - n(D_p,t)\int_0^{\infty} K(q,D_p)n(q,t)dq \tag{2}$$

where $K(D_{p1},D_{p2})$ is the coagulation kernel (*15*) between particles of diameters D_{p1} and D_{p2}.

The change in aerosol number distribution due to particle wall deposition is expressed as

$$\left(\frac{\partial n(D_p,t)}{\partial t}\right)_{wall\ loss} = -\beta(D_p)n(D_p,t) \tag{3}$$

where $\beta(D_p)$ is the size-dependent first-order loss rate coefficient. The $\beta(D_p)$ values used in the present simulations are those determined experimentally for the Caltech chamber (*16*). Particles that deposit on the wall during the course of an experiment are treated theoretically in one of two

ways for computing the SOA yield (*16*). In the so-called lower limit, once particles are lost to the walls, they are assumed to cease participation in condensation/evaporation or coagulation. The mass of condensed oxidation products on each particle at the time of its deposition is added to that of suspended particles in computing the SOA yield. The lower limit will be used in the simulations presented here. Historically, yields have also been reported using the so-called upper limit, in which particles lost to the wall are assumed to continue to participate in condensation/evaporation as if they had remained suspended. This approach includes some transfer of organic vapors to chamber walls but does not account for differences in wall versus particle transport timescales (*11*).

The rate of vapor condensation onto a spherical aerosol particle can be expressed as (*15*):

$$J_i = 2\pi D_i D_p (G_i - G_i^{eq}) F_{FS} \tag{4}$$

where G_i represents the gas-phase concentration of species i, and G_i^{eq} is the equilibrium gas-phase concentration, both expressed in $\mu g\ m^{-3}$. D_i is the molecular diffusivity of species i in air. The Fuchs-Sutugin correction for non-continuum gas-phase diffusion is (*15*)

$$F_{FS} = \frac{0.75\alpha_p(1+Kn)}{Kn^2 + Kn + 0.283Kn\alpha_p + 0.75\alpha_p} \tag{5}$$

α_p is the accommodation coefficient of the vapor species on the particle. Kn is the Knudsen number, defined as $Kn = 2\lambda_{AB}/D_p$; λ_{AB} is the mean free path of the diffusing molecule in air, given by $\lambda_{AB} = 3D_i/\bar{c}_A$; and $\bar{c}_A$ is the mean speed of the diffusing molecule, $\bar{c}_A = (8RT/\pi M_A)^{1/2}$, where R is the ideal gas constant, T is the temperature, and M_A is the molecular weight of the diffusing molecule. Numerical values for all parameters that are used in the simulations are given in Table 1. Equations 4 and 5 are applied in each size bin to calculate the condensation or evaporation flux of each vapor species to or from a single particle and then scaled by the number concentration of particles in that size bin. The flux summed over all size bins produces the rate of change of each vapor species due to evaporation or condensation.

5

The vapor-particle accommodation coefficient α_p encompasses all resistances to vapor-particle mass transfer, including surface accommodation and diffusion limitations in the particle phase (17, 18). Vapor-particle accommodation coefficients are difficult to predict from molecular properties alone, but have been measured experimentally in both thermodenuders and evaporation chamber studies (17–21). A range of values have been determined, even for the same systems. For example, Stanier et al. (19) measured evaporation rates of α-pinene SOA using tandem differential mobility analysis and found accommodation coefficients <0.1. Saleh et al. (17) measured gas-particle equilibrium timescales of α-pinene SOA in a thermodenuder and concluded the accommodation coefficient was of order 0.1. However, Lee et al. (22) measured the volatility of monoterpene SOA (including that from α-pinene), and found that depending on the heat of vaporization assumed, accommodation coefficients needed to fit evaporation rates in a thermodenuder ranged from 0.002 to 0.05. Grieshop et al. (20) used isothermal dilution to measure evaporation of α-pinene SOA, and deduced accommodation coefficients of order 0.001 to 0.01. It should be noted that the accommodation coefficients determined from these evaporation studies are not independent of the assumed volatility distribution for the SOA compounds, and may underestimate the influence of condensed phase reactions (23). For toluene SOA, Zhang et al. (11) measured SOA yields at different initial seed particle surface areas and found $\alpha_p = 0.001$ based on the observed aerosol growth; $\alpha_p = 0.001$ is used as the base value in the current simulations.

Calculation of G_i^{eq} is based on the saturation mass concentrations and the organic aerosol concentrations in the particle phase (24, 25):

$$G_i^{eq} = \frac{A_i C_i^*}{\sum_k A_k + M_{init}} \tag{6}$$

In this equation, A_i is the concentration of species i in the particle phase, C_i^* is the saturation concentration of species i, $\sum_k A_k$ is the sum of all species in the condensed phase, of which i is a subset, and M_{init} is the mass concentration of any initially present absorbing organic concentration, all expressed in terms of μg m^{-3} of air. In general, G_i^{eq} varies for each size bin, based on the mass concentration of species i and the total organic concentration in that size bin. For computational

6

convenience, owing to the presence of coagulation, the concentration of each organic species i in each size bin is not tracked dynamically; only the total condensed mass of each species over the entire size distribution is determined. The total mass in each size bin is also tracked, but this mass is not resolved into organic and inorganic masses because the number of particles in each size bin changes with time. Consequently, G_i^{eq} is calculated globally over the entire size distribution, based on the total mass of condensed species i and the total mass of condensed organics. (The total amount of species i in the condensed phase includes, as noted, the mass condensed onto particles that subsequently deposited on the wall.) We validated that this simplification of the actual size-dependent concentration dynamics captures the basic dependence of SOA yield on aerosol surface area by creating an equivalent moving bin model without coagulation, in which the total number of particles in each bin is conserved. The concentrations of each species i in each bin are then used to calculate G_i^{eq} for each bin. SOA yields predicted in this manner are virtually identical to those of the fixed bin model. A nominal (0.01 μg m^{-3}) nonvolatile initial organic seed aerosol concentration, M_{init}, is assumed to be present in the chamber regardless of initial inorganic seed number concentration merely to avoid numerical errors in Equation 6 at the first time step. Results are insensitive to this value up to 1 μg m^{-3}. Simulations (not shown) demonstrate that including the Kelvin effect in the calculation of the equilibrium vapor pressure has a negligible influence on the computed SOA yields for size distributions typical of seeded SOA chamber experiments.

Vapor wall deposition is assumed to occur for species B, C and D and is characterized by a first-order deposition coefficient, $k_{wall,on}$ (26):

$$k_{wall,on} = \left(\frac{A}{V}\right) \frac{\frac{\alpha_{wall}\bar{c}}{4}}{1.0 + \frac{\pi}{2}\left[\frac{\alpha_{wall}\bar{c}}{4(k_e D_i)^{0.5}}\right]} \tag{7}$$

where $\frac{A}{V}$ is the surface area to volume ratio of the chamber, α_{wall} is the accommodation coefficient for vapor species on the wall layer, and k_e is the coefficient of eddy diffusion that characterizes the degree of mixing in the chamber. For convenience, a single value of α_{wall} is assumed to apply for each of species B through D. The nominal value of α_{wall} is set to $1\text{x}10^{-5}$ (estimated experimentally

139 in (*9*)), and k_e = 0.015 s^{-1} (estimated for the Caltech chamber in (*11*) *SI*). These values yield

140 $k_{wall,on}$ = 1.7x10^{-4}s^{-1}, in good agreement with the optimal $k_{wall,on}$ obtained by fitting toluene

141 SOA data in Zhang et al. ($k_{wall,on}$ = 2.5x10^{-4}s^{-1} (*11*)). The value of $k_{wall,on}$ is not sensitive to

142 $\alpha_{wall} > 10^{-5}$ (see Fig. S4 of (*11*)).

143   Matsunaga and Ziemann (*9*) showed that vapor species can dissolve and equilibrate in the

144 teflon walls of conventional laboratory chambers and introduced the parameter C_w to represent the

145 capacity of teflon to take up organics. While C_w has units of concentration, it does not necessarily

146 represent a physical layer of organic material on the wall. In the present model, vapor interaction

147 with the wall is similarly assumed to be reversible, with a rate of desorption of $k_{wall,off}$ (*9*):

$$k_{wall,off} = \frac{k_{wall,on}}{K_w C_w} = k_{wall,on} \left(\frac{C_i^* M_w \gamma_w}{C_w M_p \gamma_p} \right) \tag{8}$$

148 where K_w is the vapor-wall partitioning coefficient, M_w is the effective molecular weight of the wall

149 material, γ_w is the activity coefficient of the species in the wall layer, M_p is the average molecular

150 weight of the organic species in the particle, and γ_p is the activity coefficient of the species in

151 the particle. This equation is derived using the definition $K_w = RT/M_w \gamma_w P_i^o$ and the relationship

152 $C_i^* = M_p \gamma_p P_i^o / RT$ to convert vapor pressure P_i^o into saturation concentration (*9*). For convenience,

153 we assume that $M_w = M_p$ and $\gamma_p = \gamma_w$ (*11*). As noted, the saturation concentration C_i^* is taken

154 to decrease progressively by one order of magnitude for species B through D. The nominal value

155 for C_w is set at 10 mg m^{-3}, based on observations of Matsunaga and Ziemann (*9*) that C_w varies

156 between 2 and 24 mg m^{-3} for different compounds.

Numerical Experiments

158 The coupled vapor-aerosol dynamics-wall model is used to explore the sensitivity of SOA yield

159 to vapor wall deposition. The assumed seed aerosol size distribution is based on typical distribu-

160 tions in the Caltech laboratory chamber, encompassing 53 size bins, spanning the diameter range

161 from 15 to 800 nm and log-normal with a standard deviation of 1.5. The initial particle number

concentration is varied for different simulations in order to vary the total initial seed surface area. For each combination of parameters, seven different initial particle number concentrations, given in Table 2, are used in order to generate seven initial seed surface areas. The ratio of the initial seed surface area to the surface area of the chamber walls, based on the Caltech laboratory chambers, is also given in Table 2 for each case. The estimated surface area of the Caltech chamber is 41 m^2 assuming a rectangular shape with sides of 2.74 m, 2.43 m, and 2.69 m. Each simulation is run for 20 h of oxidation, and the SOA yield is calculated at the end of each simulation.

The parameters used in each simulation are given in Table 1. For $k[\text{OH}]_{A \rightarrow B}$, the base value is assigned as 10^{-5} s^{-1} to represent the product of the toluene-OH rate constant of 5.6x10^{-12} cm^3 molec^{-1} s^{-1} and an OH concentration of ≈ 2x10^6 molec cm^{-3}, the approximate value observed during the toluene SOA experiments in (*11*). The $k[\text{OH}]$ for each successive reaction, B$\rightarrow$C, etc., is assumed to be five times the previous $k[\text{OH}]$ in order to approximate the increase in reaction rate as species become more oxidized. Results are insensitive to this reaction rate scaling factor for values between 1 and 5. α_p is varied from 0.001, the best fit value determined by (*11*), to 1, ideal accommodation. The saturation concentrations for species B through D are set as [10^1 10^0 10^{-1}] μg m^{-3}.

Results and Discussion

Increased partitioning vs. wall deposition effect

The clear increase in SOA yield observed by Zhang et al. (*11*) with increased seed particle surface area can arise from two separate effects: (1) Increased organic aerosol concentration C_{OA} via gas-particle partitioning if condensation is kinetically limited; and (2) Reduction in the deposition of vapor organics to the wall. To evaluate these separate, but potentially overlapping, effects, numerical experiments were performed with different α_p values and in the presence or absence of vapor wall deposition at varying initial seed surface areas. Figure 1 shows C_{OA} at the end of 20 h numerical experiments starting with a parent VOC mixing ratio of 40 ppb (concentration G_{A0} 327

9

μg m^{-3}). Pie charts are shown giving the distribution of products in the organic aerosol phase at the end of the simulations for the highest initial seed surface area. For $\alpha_p = 0.001$, C_{OA} increases as surface area increases both in the presence and absence of vapor wall deposition. The surface area dependence of C_{OA} even in the absence of vapor wall deposition indicates that the observation of surface area-dependent yields is not sufficient to prove the existence of vapor wall deposition.

The increase in C_{OA} in both the presence and absence of wall deposition is attributable to the kinetic limitations on organic vapor condensation on particles imposed by a low value of α_p. This limitation is illustrated by comparing the characteristic timescale for gas-particle equilibration with the timescales for reaction and wall deposition (Figure 2). The characteristic timescale for gas-particle equilibration $\tau_{g,p}$ (i.e. the *e*-folding time for an aerosol to reestablish vapor-particle equilibrium after a slight perturbation) is (*15*)

$$\tau_{g,p} = \frac{1}{2\pi D_i (\sum_{bins} n(D_p) D_p F_{FS})} \tag{9}$$

This timescale is not necessarily that for vapor and particle phases to establish equilibrium in an SOA formation experiment, which depends on other factors such as the rate of reaction and the volatilities of the products (*27*). In Figure 2, $\tau_{g,p}$ is calculated based on the initial size distribution, but its value will change with time as $n(D_p)$ in each size bin evolves (as discussed below). Quasi-equilibrium growth occurs when the net production rate of condensable vapors is slow compared to the time to establish gas-particle equilibrium; in this limit, the vapor and particle phases maintain equilibrium (*28, 29*). The magnitude of $\tau_{g,p}$ relative to timescales for other processes in the system governs the transition between kinetically-limited and quasi-equilibrium growth (*28*). Gas-particle equilibrium is governed by the total organic mass in the system and is not dependent on the surface area of the inorganic seed. In contrast, kinetically-limited condensation, when $\tau_{g,p}$ is competitive with the timescale for production of condensable vapors, depends on the aerosol surface area. The reaction timescale τ_{rxn} controls the production rate of condensable vapors. In Figure 2, τ_{rxn} is calculated based on $k[\text{OH}]_{C \rightarrow D}$ because this reaction controls the production rate for the least volatile species. For $\alpha_p = 0.001$, $\tau_{g,p}$ exceeds τ_{rxn} at the lowest seed surface areas, indicating that

10

condensation is kinetically limited, and C_{OA} for $\alpha_p = 0.001$ in the absence of wall deposition in Figure 1 consequently increases sharply with seed surface area. As the seed surface area increases at $\alpha_p = 0.001$, $\tau_{g,p}$ becomes an order of magnitude smaller than τ_{rxn}, and C_{OA} achieves a plateau at the highest seed surface areas. As α_p increases, $\tau_{g,p}$ decreases with respect to τ_{rxn} and condensation shifts towards quasi-equilibrium growth. This shift is evident in Figure 1, as C_{OA} in the absence of wall deposition becomes less dependent on seed surface area as α_p increases.

The presence of vapor wall deposition introduces an additional timescale into the system, $\tau_{g,w} = 1/k_{wall,on}$, the characteristic timescale of vapor wall deposition. $\tau_{g,p}$ must be $< \tau_{rxn}$ and $\tau_{g,w}$ for quasi-equilibrium growth. When $\tau_{rxn} \approx \tau_{g,w}$, C_{OA} in the presence of vapor wall deposition becomes less dependent on seed surface area as α_p increases. Ehn et al. (*30*) observed SOA yields from the ozonolysis of α-pinene to increase with increasing particle surface area but required $\alpha_p = 1.0$ to fit the observed growth data. The observed vapor wall deposition rate was much greater in their continuously stirred reactor than that in the Caltech chamber (0.011 s^{-1} versus 2.5x10^{-4} s^{-1}). In their reactor, $\tau_{g,p} \approx \tau_{g,w}$ even at $\alpha_p = 1.0$, and condensation is kinetically limited. The presence of vapor wall deposition depresses the SOA yield from that calculated in the absence of wall deposition regardless of the value of α_p, as seen in Figure 1.

Condensation that is kinetically-limited produces a narrowing of the particle size distribution, while condensation dominated by quasi-equilibrium growth produces a broadening of the size distribution (*28, 29*). If condensation shifts towards quasi-equilibrium growth as seed surface area is increased, the evolution of the particle size distribution should theoretically reflect this shift. However, as seed surface area is increased, coagulation will become more important and may mask any broadening of the size distribution, as smaller particles are scavenged by larger particles.

Particle distributions shown in the pie charts to the right of Figure 1 demonstrate another effect of changing the gas-particle equilibration time: decreasing $\tau_{g,p}$ by increasing α_p shifts the product distribution towards earlier generation products. As $\tau_{g,p}$ decreases, partitioning of species B to the particle increases preferentially relative to conversion to C and (in the presence of wall deposition) deposition to the walls.

Yields as a function of C_{OA} at a constant temperature have historically been parameterized for use in air quality models (AQMs) such as CMAQ (*31*) with models such as the two-product model and the volatility basis set (VBS) (*32*), each of which assumes instantaneous gas-particle equilibrium. As shown in Figure 1, for $\alpha_p = 0.001$ in this system, condensation is kinetically limited. Consequently, yields simulated starting with varying G_{A0} and at varying seed surface areas cannot be described by a single two-product or VBS fit (Figure 3). The points in Figure 3 were generated by varying both G_{A0} and seed surface area with (circles) and without (diamonds) vapor wall deposition. The size of the markers increases as G_{A0} increases and colors correspond to different values of the initial seed surface area. For simplicity, the lines were generated by fitting a two-product model to the datapoints. (This fit merely illustrates the discrepancy between the simulation results and common partitioning model predictions.) For a fixed G_{A0} (indicated in Figure 3 by markers of the same size), the SOA yield increases as both C_{OA} and seed surface area increase. At a fixed seed surface area, the yield increases as G_{A0} and C_{OA} increase. For a fixed final C_{OA} (visualized by drawing vertical lines in Figure 3), the yield increases as seed surface area increases and G_{A0} *decreases*. As a result of the kinetic limitation imposed by the low α_p, the yields depend on G_{A0} in addition to the seed surface area because the time required to reach a fixed C_{OA} depends on both parameters. As surface area increases, the same final C_{OA} is achieved with decreasing G_{A0}, and the lower ΔVOC results in a higher yield.

By constrast, Figure S1 shows simulations with $\alpha_p = 0.01$, i.e. 10x larger. In the absence of vapor wall deposition, condensation shifts towards quasi-equilibrium growth with the higher α_p, and the yields approach a single curve with little seed area dependence. Yields calculated in the presence of vapor wall deposition for $\alpha_p = 0.01$ maintain a seed surface area dependence at low seed surface areas but lose this dependence at the highest surface areas. If a similar plot is generated for $\alpha_p = 1.0$ (not shown), yields in the presence and absence of wall deposition collapse onto single (but separate) curves. This further illustrates that yields increase as seed surface area increases only when condensation is kinetically limited.

12

Influence of volatility distributions

The simulations are based on saturation concentrations that decrease by an order of magnitude per each generation of reaction. Different combinations of saturations concentrations were also used with $\alpha_p = 0.001$: $C_B^* = 10^2 \ \mu$g m^{-3} with subsequent saturation concentrations decreasing by an order of magnitude per generation, $C_B^* = 10^2$ or $10^3 \ \mu$g m^{-3} with subsequent saturation concentrations decreasing by two orders of magnitude per generation, and all saturation concentrations set to zero. Each combination produces similar dependence of yield on seed surface area and a depression of the yield due to vapor wall deposition (not shown). Saturation concentrations were also varied to determine if the observed behavior of Zhang et al. (*11*) could be qualitatively reproduced using the present model. Figure S2-Figure S5 show that the behavior can be reproduced, supporting the simplifications employed in the model. More discussion is given in the Supporting Information.

Influence of reaction timescale

It has been observed experimentally that SOA yields are higher at faster oxidation rates, as the impact of vapor wall deposition is lessened (*33*). In Figure 4, $k[\text{OH}]_{A \to B}$ is increased by an order of magnitude (with $k[\text{OH}]_{B \to C}$ and $k[\text{OH}]_{C \to D}$ again five times the previous $k[\text{OH}]$), and yields are shown after 20 h of simulation (ΔVOC will necessarily vary with $k[\text{OH}]_{A \to B}$ because the simulations are run for the equivalent amount of time rather than equivalent amount of OH exposure). For $k[\text{OH}]_{A \to B} = 10^{-4}\text{s}^{-1}$ in the absence of vapor wall deposition, the yield is approximately 1.0 regardless of seed surface area. The lack of dependence of yield on surface area seems to contradict the earlier discussion of kinetically-limited versus quasi-equilibrium condensational growth: because increasing $k[\text{OH}]_{A \to B}$ decreases τ_{rxn} with respect to $\tau_{g,p}$, the system should become more kinetically-limited and show a stronger dependence on seed surface area. However, this effect is observed only if yields are considered at equivalent OH exposure times (see Figure S6). For $k[\text{OH}]_{A \to B} = 10^{-4}\text{s}^{-1}$ in a 20 h simulation, species A is virtually depleted after 15 h. In the absence of vapor wall deposition, the total concentration of condensable vapors (species B through

D) is no longer changing except via condensation. Condensation will therefore be governed by quasi-equilibrium growth and is independent of seed surface area. In the presence of vapor wall deposition, SOA yields maintain the surface area dependence for $k[\text{OH}]_{A \to B} = 10^{-4}\text{s}^{-1}$ because vapor wall deposition causes condensation to remain kinetically limited throughout the experiment.

This analysis reveals the subtleties in comparing yields measured under different experimental conditions such as different OH levels, because the effects of both kinetic condensation limitations and vapor wall deposition will change with both the rate of oxidation and the duration of an experiment.

Evolution of $\tau_{g,p}$

The preceding analysis has been based on an assumed initial seed aerosol size distribution: yields are determined as a function of the initial seed surface area, and $\tau_{g,p}$ (Figure 2) is calculated based on the initial size distribution. The aerosol size distribution changes continuously as particles grow by condensation and are lost by coagulation or wall deposition. To examine the extent to which the initial size distribution is a robust metric for comparing different experimental conditions, we consider the time evolution of $\tau_{g,p}$ for $\alpha_p = 0.001$ with vapor wall deposition at each initial seed surface area (Figure S7). $\tau_{g,p}$ increases by approximately half an order of magnitude for all seed surface areas considered but remains within roughly one order of magnitude of $\tau_{g,w}$, for which vapor wall deposition and vapor condensation remain competitive. Furthermore, differences in the values of $\tau_{g,p}$ between different intial seed surface areas remain similar throughout the simulation. These results indicate that although vapor condensation may become more kinetically-limited as the oxidation progresses, the initial seed aerosol size distribution is a robust metric for comparing oxidation trajectories.

Vapor Wall Deposition Bias in SOA Yield

Figure 1-Figure 4 indicate that the mere increase of SOA yield as seed surface area increases does not, in itself, prove that vapor wall deposition is occurring. Furthermore, separating the impacts

14

of condensational kinetic limitations and vapor wall deposition is not straightforward. Zhang et al. (*11*) introduced the concept of a wall deposition bias R_{wall},

$$R_{wall} = \frac{Y^0}{Y} \tag{10}$$

the ratio of the SOA yield in the absence of wall deposition, Y^0, to that obtained in an equivalent experiment with wall deposition, Y. R_{wall} is shown as a function of the seed surface area in Figure 5 for $\alpha_p = 0.001, 0.01,$ and 1. For $\alpha_p = 0.001$ (and to a lesser extent $\alpha_p = 0.01$), R_{wall} decreases as the seed surface area increases and then reaches a plateau, as observed experimentally in (*11*). The analysis presented here suggests that the behavior of R_{wall} at low surface areas is influenced by the kinetic limitations that are a consequence of a small α_p. Furthermore, R_{wall} changes with $k[\text{OH}]_{A\to B}$ and G_{AO} because these parameters affect yields calculated both in the presence and absence of vapor wall deposition.

The multi-faceted dependencies of SOA yield and R_{wall} complicate the extrapolation of chamber-derived yields to atmospheric models. If condensation in the atmosphere is dominated by quasi-equilibrium growth, chamber experiments should be carried out, if possible, at high seed surface areas, with high G_{AO} and under rapid oxidation conditions, to minimize the effects of both kinetic limitations and vapor wall deposition. If, however, condensation in the atmosphere is also kinetically limited, chamber experiments can be conducted at seed concentrations typical of those in the atmosphere and a vapor-particle dynamics model, similar to those presented here and in (*11*), can be used in order to correct for vapor wall deposition. Thus, challenges will need to be met in designing experiments that simultaneously minimize the magnitude of vapor deposition to the chamber walls yet ensure conditions similar to those encountered in the ambient atmosphere. The strong sensitivity of R_{wall} to the value of the vapor-particle accommodation coefficient α_p points to a need for constraining the value of this parameter, establishing the extent to which it varies among different chemical systems and under differing reaction conditions, and ultimately determining a value most relevant for the atmosphere.

15

Effect of Semi-solid SOA

The present simulations do not explicitly address the microphysical nature of the particles. Recent evidence suggests that SOA often exists in a semi-solid state (e.g. (*34*, *35*)). In such a case, $\tau_{g,p}$ increases relative to $\tau_{g,w}$ and τ_{rxn} (*28*). Retarded gas-particle partitioning resulting from condensed phase diffusion limitations will drive the system towards kinetically-limited SOA growth, and is essentially captured by α_p values < 1. Overall particle growth is dictated by accommodation into the particle bulk and is thus sensitive to limitations imposed by particle phase morphology. The results here demonstrate that the dependence of both the SOA yield and R_{wall} on seed surface area is important only when SOA growth is kinetically limited. This suggests that SOA systems in which the SOA exists in a semi-solid state may exhibit a stronger seed surface area dependence and may exhibit larger wall biases than those for which the SOA is more liquid-like (i.e. in which bulk accommodation is not a retarding factor).

Acknowledgement

Supporting Information Available

Figures S1-S7 are provided in the Supporting Information. This material is available free of charge via the Internet at `http://pubs.acs.org`.

Table 1: Simulation Parameters

Parameter	Definition	Value
α_p	Accommodation coefficient of vapor species on particle	Varied
A/V	Surface-area-to-volume ratio of the chamber	1.6 m^{-1}
α_{wall}	Accommodation coefficient of vapor species on the wall	10^{-5}
C_i^*	Saturation concentrations for species B through D	$[10^1 \ 10^0 \ 10^{-1}] \ \mu\text{g m}^{-3}$
C_w	Equivalent wall organic aerosol concentration	10 mg m^{-3}
D_i	Gas-phase diffusivity of species i	$3\text{x}10^{-6} \text{ m}^2 \text{ s}^{-1}$
G_{A0}	Initial parent VOC concentration	$327 \ \mu\text{g m}^{-3}$ (40 ppb)
k_e	Coefficient of eddy diffusion in chamber	0.015 s^{-1}
$k[\text{OH}]_{A \rightarrow B}$	Product of reaction rate constant and OH concentration	10^{-5} s^{-1}
$k_{wall,on}$	First-order vapor wall deposition coefficient	$1.7\text{x}10^{-4} \text{ s}^{-1}$
M_i	Species molecular weight	200 g mol^{-1}
M_{init}	Initially absorbing organic material in seed aerosol	$0.01 \ \mu\text{g m}^{-3}$
P	Pressure	$1\text{x}10^5 \text{ Pa}$
ρ	Particle density	1700 kg m^{-3}
T	Temperature	298 K

Table 2: Assumed Initial Aerosol Number Distribution Parameters

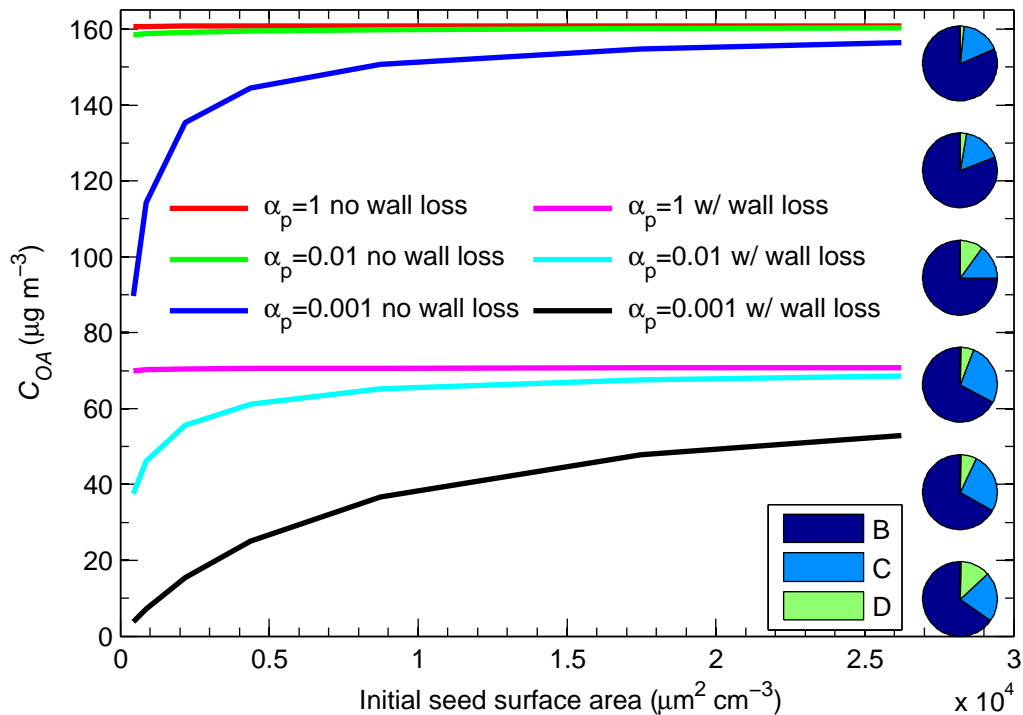| Case	Initial particle concentration (cm^{-3})	Mean particle diameter (nm)	Initial particle surface area (μm^2 cm^{-3})	Ratio of initial particle SA to wall SA
1	10,000	100	$4.4\text{x}10^2$	$2.7\text{x}10^{-4}$
2	20,000	100	$8.7\text{x}10^2$	$5.3\text{x}10^{-4}$
3	50,000	100	$2.2\text{x}10^3$	$1.3\text{x}10^{-3}$
4	100,000	100	$4.4\text{x}10^3$	$2.7\text{x}10^{-3}$
5	200,000	100	$8.7\text{x}10^3$	$5.3\text{x}10^{-3}$
6	400,000	100	$1.7\text{x}10^4$	$1.1\text{x}10^{-2}$
7	600,000	100	$2.6\text{x}10^4$	$1.6\text{x}10^{-2}$

Figure 1: Final organic aerosol concentration C_{OA} after 20 h of simulation as a function of the initial seed surface area for simulations beginning with 40 ppb of parent VOC. Conditions for the simulations are given in Table 1 and Table 2. Different combinations of α_p and presence or absence of wall deposition are shown. The pie charts at the right show the product distribution at the end of the simulation at the highest seed surface area considered for each of the six simulations. The pie charts appear top to bottom in the same top-to-bottom order as the C_{OA} curves.
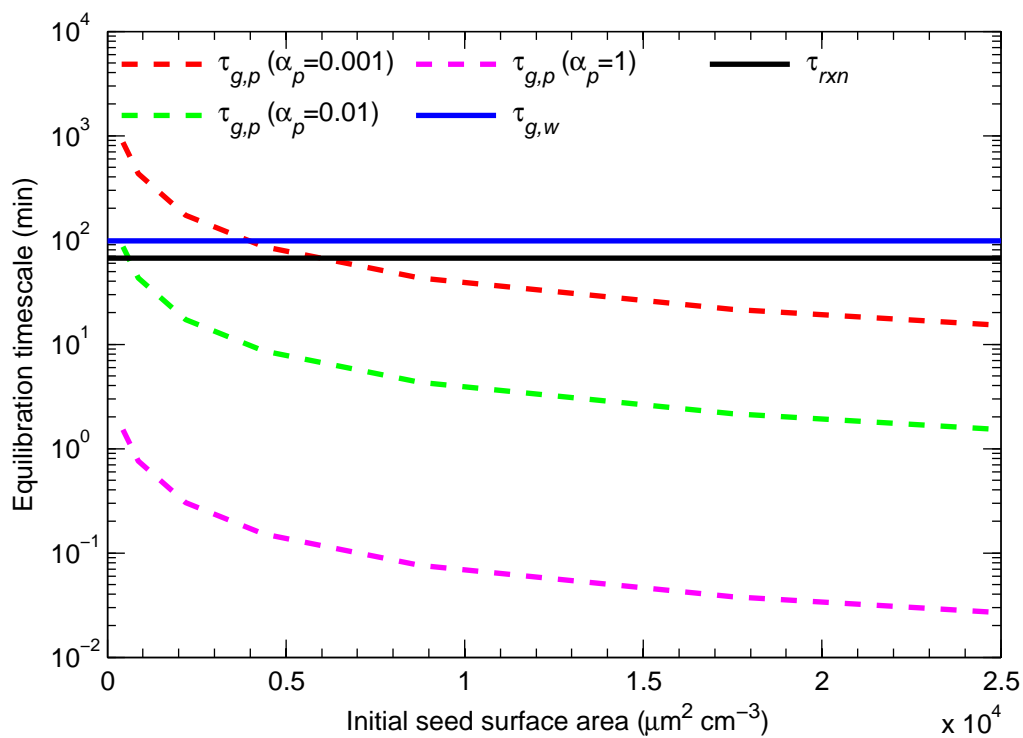
Figure 2: Equilibration timescale for gas-particle partitioning as a function of the initial seed surface area for different values of the vapor-particle accommodation coefficient, α_p. The equilibration timescale for gas-wall partitioning ($\tau_{g,w} = 1/k_{wall,on}$) and the timescale for reaction ($\tau_{rxn} = 1/(k[\text{OH}]_{C \rightarrow D})$) are shown as horizontal lines as these timescales are independent of seed surface area.
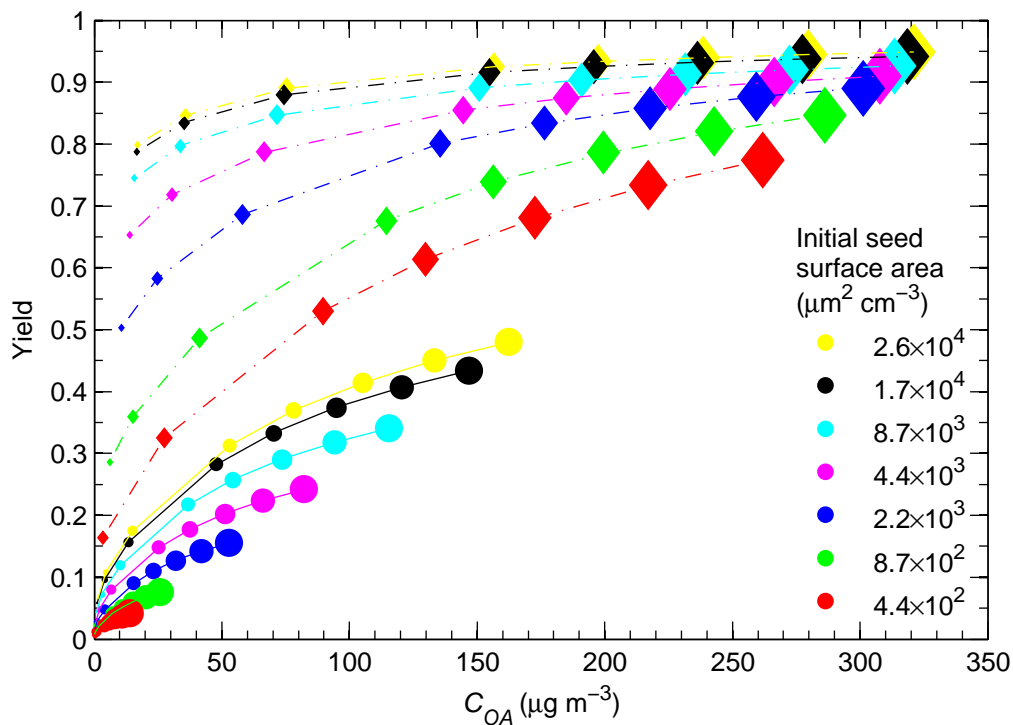
Figure 3: SOA yields after 20 h of simulation as a function of the final organic aerosol concentration C_{OA} for $\alpha_p = 0.001$. The points on the curve were generated by varying the initial parent VOC concentration G_{A0} with (circles) and without (diamonds) vapor wall deposition. The size of the markers increases as G_{A0} increases and colors correspond to different values of the initial seed surface area. The lines were generated by fitting a two-product model to the datapoints.
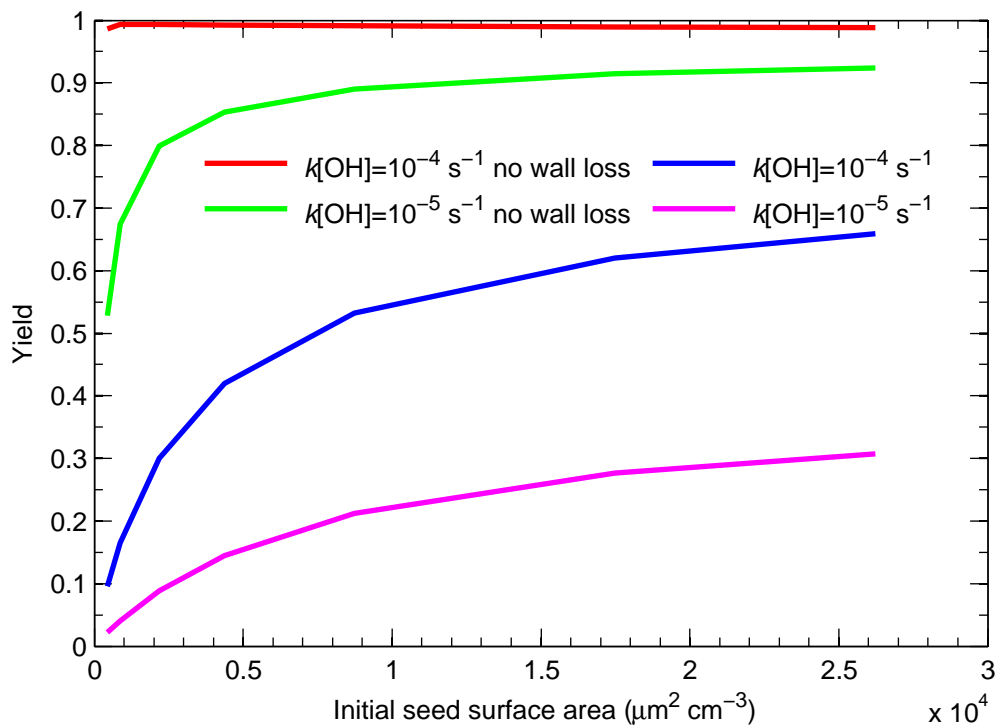
Figure 4: SOA yields after 20 h of simulation as a function of the initial seed surface area for simulations with $\alpha_p = 0.001$ for different values of $k[\text{OH}]_{A \to B}$, in the presence and absence of wall deposition.
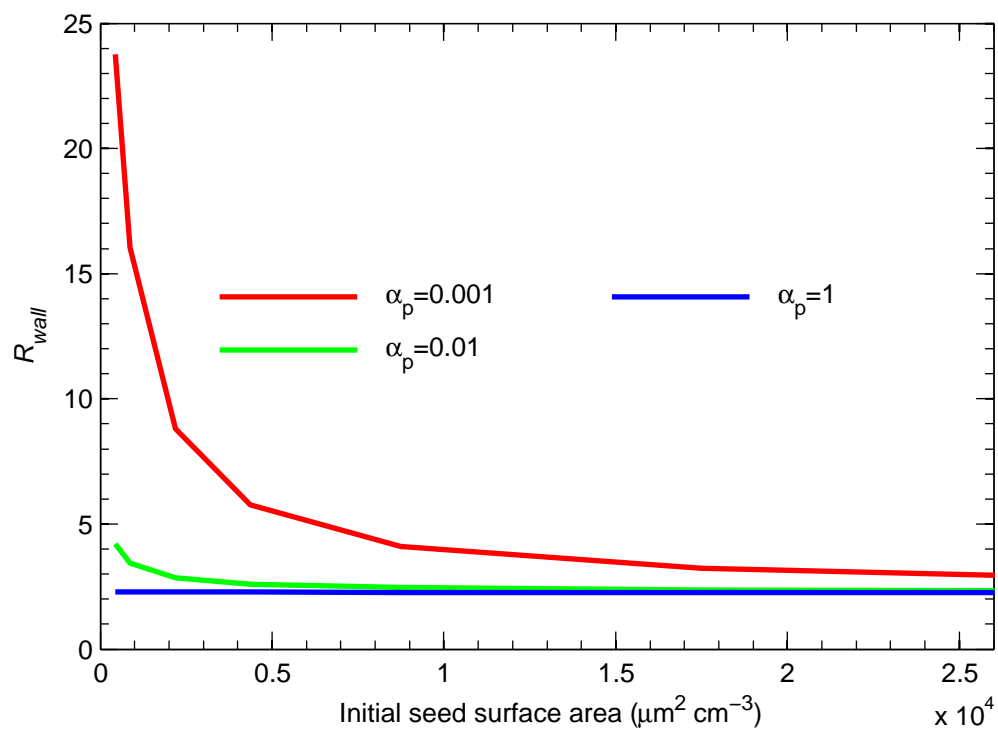
Figure 5: Wall deposition bias, $R_{wall} = Y^0/Y$, as a function of the initial seed surface area at different values of the vapor-particle accommodation coefficient α_p with an initial VOC mixing ratio of 40 ppb and $k[\text{OH}]_{A \rightarrow B} = 10^{-5}$ s^{-1}.

References

(1) Ensberg, J. J.; Hayes, P. L.; Jimenez, J. L.; Gilman, J. B.; Kuster, W. C.; de Gouw, J. A.; Holloway, J. S.; Gordon, T. D.; Jathar, S.; Robinson, A. L.; Seinfeld, J. H. Emission factor ratios, SOA mass yields, and the impact of vehicular emissions on SOA formation. *Atmos. Chem. Phys.* **2014**, *14*, 2383–2397, doi:10.5194/acp-14-2383-2014.

(2) de Gouw, J. A.; Middlebrook, A. M.; Warneke, C.; Goldan, P. D.; Kuster, W. C.; Roberts, J. M.; Fehsenfeld, F. C.; Worsnop, D. R.; Canagaratna, M. R.; Pszenny, A. A. P.; Keene, W. C.; Marchewka, M.; Bertman, S. B.; Bates, T. S. Budget of organic carbon in a polluted atmosphere: Results from the New England Air Quality Study in 2002. *J. Geophys. Res.-Atmos.* **2005**, *110*, 27781–27794.

(3) Volkamer, R.; Jimenez, J. L.; San Martini, F.; Dzepina, K.; Zhang, Q.; Salcedo, D.; Molina, L. T.; Worsnop, D. R.; Molina, M. J. Secondary organic aerosol formation from anthropogenic air pollution: rapid and higher than expected. *Geophys. Res. Lett.* **2006**, *33*.

(4) Johnson, D.; Utembe, S. R.; Jenkin, M. E.; Derwent, R. G.; Hayman, G. D.; Alfarra, M. R.; Coe, H.; McFiggans, G. Simulating regional scale secondary organic aerosol formation during the TORCH 2003 campaign in the southern UK. *Atmos. Chem. Phys.* **2006**, *6*, 403-418.

(5) de Gouw, J. A.; Brock, C. A.; Atlas, E. L.; Bates, T. S.; Fehsenfeld, F. C.; Goldan, P. D.; Holloway, J. S.; Kuster, W. C.; Lerner, B. M.; Matthew, B. M.; Middlebrook, A. M.; Onasch, T. B.; Peltier, R. E.; Quinn, P. K.; Senff, C. J.; Stohl, A.; Sullivan, A. P.; Trainer, M.; Warneke, C.; Weber, R. J.; Williams, E. J. Sources of particulate matter in the northeastern United States in summer: 1. Direct emissions and secondary formation of organic matter in urban plumes. *J. Geophys. Res.-Atmos.* **2008**, *113*, 27781.

(6) Kleinman, L. I.; Springston, S. R.; Daum, P. H.; Lee, Y.-N.; Nunnermacker, L. J.; Senum, G. I.; Wang, J.; Weinstein-Lloyd, J.; Alexander, M. L.; Hubbe, J.; Ortega, J.; Canagaratna, M. R.;

23

Jayne, J. The time evolution of aerosol composition over the Mexico City plateau. *Atmos. Chem. Phys.* **2008**, *8*, 1559–1575.

(7) Matsui, H.; Koike, M.; Takegawa, N.; Kondo, Y.; Griffin, R. J.; Miyazaki, Y.; Yokouchi, Y.; Ohara, T. Secondary organic aerosol formation in urban air: temporal variations and possible contributions from unidentified hydrocarbons. *J. Geophys. Res.-Atmos.* **2009**, *114*.

(8) Loza, C. L.; Chan, A. W.; Galloway, M. M.; Keutsch, F. N.; Flagan, R. C.; Seinfeld, J. H. Characterization of vapor wall loss in laboratory chambers. *Environ. Sci. Technol.* **2010**, *44*, 5074–5078.

(9) Matsunaga, A.; Ziemann, P. J. Gas-wall partitioning of organic compounds in a teflon film chamber and potential effects on reaction product and aerosol yield measurements. *Aerosol Sci. Technol.* **2010**, *44*, 881–892.

(10) Pathak, R.; Donahue, N. M.; Pandis, S. N. Ozonolysis of β-pinene: Temperature dependence of secondary organic aerosol mass fraction. *Environ. Sci. Technol.* **2008**, *42*, 5081–5086.

(11) Zhang, X.; Cappa, C. D.; Jathar, S. H.; McVay, R. C.; Ensberg, J. J.; Kleeman, M. J.; Seinfeld, J. H. Influence of vapor wall-loss in laboratory chambers on yields of secondary organic aerosol. *Proc. Natl. Acad. Sci.* **2014**, *111*, 5802–5807, doi:10.1073/pnas.1404727111.

(12) Cappa, C. D.; Wilson, K. R. Multi-generation gas-phase oxidation, equilibrium partitioning, and the formation and evolution of secondary organic aerosol. *Atmos. Chem. Phys.* **2012**, *12*, 9505–9528.

(13) Cappa, C. D.; Zhang, X.; Loza, C. L.; Craven, J. S.; Yee, L. D.; Seinfeld, J. H. Application of the Statistical Oxidation Model (SOM) to secondary organic aerosol formation from photooxidation of C12 alkanes. *Atmos. Chem. Phys.* **2013**, *13*, 1591–1606.

(14) Pierce, J. R.; Engelhart, G. J.; Hildebrandt, L.; Weitkamp, E. A.; Pathak, R. K.; Donahue, N. M.; Robinson, A. L.; Adams, P. J.; Pandis, S. N. Constraining particle evolution

410   from wall losses, coagulation and condensation-evaporation in smog-chamber experiments: Optimal estimation based on size distribution measurements. *Aerosol Sci. Technol.* **2008**, *42*, 1001-1015.

(15) Seinfeld, J. H.; Pandis, S. N. *Atmospheric chemistry and physics: from air pollution to climate change*, 2nd ed. Wiley: Hoboken, N.J., 2006.

(16) Loza, C. L.; Chhabra, P. S.; Yee, L. D.; Craven, J. S.; Flagan, R. C.; Seinfeld, J. H. Chemical aging of m-xylene secondary organic aerosol: laboratory chamber study. *Atmos. Chem. Phys.* **2012**, *12*, 151–167.

(17) Saleh, R.; Donahue, N. M.; Robinson, A. L. Time scales for gas-particle partitioning equilibration of secondary organic aerosol formed from alpha-pinene ozonolysis. *Environ. Sci. Technol.* **2013**, *47*, 5588-5594.

(18) Vaden, T. D.; Imre, D.; Beranek, J.; Shrivastava, M.; Zelenyuk, A. Evaporation kinetics and phase of laboratory and ambient secondary organic aerosol. *Proc. Natl. Acad. Sci.* **2011**, *108*, 2190-2195.

(19) Stanier, C. O.; Pathak, R. K.; Pandis, S. N. Measurements of the volatility of aerosols from alpha-pinene ozonolysis. *Environ. Sci. Technol.* **2007**, *41*, 2756-2763.

(20) Grieshop, A. P.; Donahue, N. M.; Robinson, A. L. Is the gas-particle partitioning in alpha-pinene secondary organic aerosol reversible? *Geophys. Res. Lett.* **2007**, *34*, L14810.

(21) Pierce, J. R.; Riipinen, I.; Kulmala, M.; Ehn, M.; Petaja, T.; Junninen, H.; Worsnop, D. R.; Donahue, N. M. Quantification of the volatility of secondary organic compounds in ultrafine particles during nucleation events. *Atmos. Chem. Phys.* **2011**, *11*, 9019-9036.

(22) Lee, B. H.; Pierce, J. R.; Engelhart, G. J.; Pandis, S. N. Volatility of secondary organic aerosol from the ozonolysis of monoterpenes. *Atmos. Environ.* **2011**, *45*, 2443–2452.

(23) Trump, E. R.; Donahue, N. M. Oligomer formation within secondary organic aerosols: equilibrium and dynamic considerations. *Atmos. Chem. Phys.* **2014**, *14*, 3691-3701.

(24) Pankow, J. F. An absorption model of gas/particle partitioning of organic compounds in the atmosphere. *Atmos. Environ.* **1994**, *28*, 185–188.

(25) Bowman, F. M.; Odum, J. R.; Seinfeld, J. H.; Pandis, S. N. Mathematical model for gas-particle partitioning of secondary organic aerosols. *Atmos. Environ.* **1997**, *31*, 3921–3931.

(26) McMurry, P. H.; Grosjean, D. Gas and aerosol wall losses in teflon film smog chambers. *Environ. Sci. Technol.* **1985**, *19*, 1176–1182.

(27) Riipinen, I.; Pierce, J. R.; Donahue, N. M.; Pandis, S. N. Equilibration time scales of organic aerosol inside thermodenuders: Evaporation kinetics versus thermodynamics. *Atmos. Environ.* **2010**, *44*, 597–607.

(28) Shiraiwa, M.; Seinfeld, J. H. Equilibration timescale of atmospheric secondary organic aerosol partitioning. *Geophys. Res. Lett.* **2012**, *39*, L24801.

(29) Zhang, X.; Pandis, S. N.; Seinfeld, J. H. Diffusion-limited versus quasi-equilibrium aerosol growth. *Aerosol Sci. Technol.* **2012**, *46*, 874-885.

(30) Ehn, M.; Thornton, J. A.; Kleist, E.; Sipila, M.; Junninen, H.; Pullinen, I.; Springer, M.; Rubach, F.; Tillmann, R.; Lee, B.; et al. A large source of low-volatility secondary organic aerosol. *Nature* **2014**, *506*, 476.

(31) Carlton, A. G.; Bhave, P. V.; Napelenok, S. L.; Edney, E. D.; Sarwar, G.; Pinder, R. W.; Pouliot, G. A.; Houyoux, M. Model representation of secondary organic aerosol in CMAQv4.7. *Environ. Sci. Technol.* **2010**, *44*, 8553-8560.

(32) Presto, A. A.; Donahue, N. M. Investigation of α-pinene + ozone secondary organic aerosol formation at low total aerosol mass. *Environ. Sci. Technol.* **2006**, *40*, 3536–3543.

(33) Ng, N. L.; Kroll, J. H.; Chan, A. W. H.; Chhabra, P. S.; Flagan, R. C.; Seinfeld, J. H. Secondary organic aerosol formation from *m*-xylene, toluene, and benzene. *Atmos. Chem. Phys.* **2007**, *7*, 3909-3922.

(34) Virtanen, A.; Joutsensaari, J.; Koop, T.; Kannosto, J.; Yli-Pirila, P.; Leskinen, J.; Makela, J. M.; Holopainen, J. K.; Poschl, U.; Kulmala, M.; Worsnop, D. R.; Laaksonen, A. An amorphous solid state of biogenic secondary organic aerosol particles. *Nature* **2010**, *467*, 824-827.

(35) Saukko, E.; Lambe, A. T.; Massoli, P.; Koop, T.; Wright, J. P.; Croasdale, D. R.; Pedernera, D. A.; Onasch, T. B.; Laaksonen, A.; Davidovits, P.; Worsnop, D. R.; Virtanen, A. Humidity-dependent phase state of SOA particles from biogenic and anthropogenic precursors. *Atmos. Chem. Phys.* **2012**, *12*, 7517-7529.

Supporting Information for:

Vapor Wall Deposition in Chambers: Theoretical Considerations

Renee C. McVay, Christopher D. Cappa, John H. Seinfeld*

*Correspondence to John H. Seinfeld, seinfeld@caltech.edu

Contents: Figures S1-S7

Comparison to Zhang et al. (*11*)

The SOA growth data from Zhang et al. (*11*) can be plotted similarly to Figure 3 and Figure S1 to observe the competing effects of kinetic limitations and vapor wall deposition. The yields over the course of each toluene low-NO_x photooxidation experiment in (*11*) are shown as circles in Figure S2 as a function of C_{OA} for different seed surface areas. The lines in Figure S2 are yields calculated using the SOM model with parameters fit to the experimental data at each surface area but in the absence of vapor wall deposition (see *SI* of (*11*) for more details). Yields over the course of one representative experiment from Ng et al. (*33*) are shown as diamonds for comparison. The measured yields from Zhang et al. (*11*) quickly reach a plateau with respect to C_{OA}, indicating that the SOA formed via the low-NO_x pathway is essentially nonvolatile for $C_{OA} > 10 \ \mu g \ m^{-3}$. These yield curves clearly diverge at different surface areas, due to both vapor wall deposition and kinetic growth limitations. Yields calculated in the absence of vapor wall deposition diverge into separate curves solely as a result of kinetic limitations on particle growth. These yields are higher than the measured yields because species that would have otherwise condensed to the walls are able to partition to particles. The model presented here qualitatively reproduces this behavior, Figure S3. To match the nonvolatile behavior observed in the low-NO_x case of (*11*), the saturation concentrations of species B through D are all decreased to $10^{-3} \ \mu g \ m^{-3}$. The magnitudes of the yields clearly differ from (*11*), but the general behavior is reproduced.

Yields over the course of each toluene high-NO_x photooxidation experiment in (*11*) are shown in Figure S4, circles representing observed yields and lines representing calculated yields from the SOM model in the absence of vapor wall deposition. Although the yield curves as a function of C_{OA} do diverge slightly, the effect is much less pronounced than in the low-NO_x case. Furthermore, the yields do not reach a plateau with respect to C_{OA}. To match this observed behavior, Figure S5, the saturation concentrations of species B through D are set as $[10^3 \ 10^1 \ 10^{-1}] \ \mu g \ m^{-3}$. The reaction rate constants are set as $k[OH]_{A \rightarrow B} = k[OH]_{B \rightarrow C} = 5 \text{x} 10^{-5} \ s^{-1}$ and $k[OH]_{C \rightarrow D} = 5 \text{x} 10^{-4} \ s^{-1}$. These parameters do not necessarily represent volatilities or rates of the toluene high-NO_x experiments in (*11*), but merely to show that the present model can reproduce the general behavior.
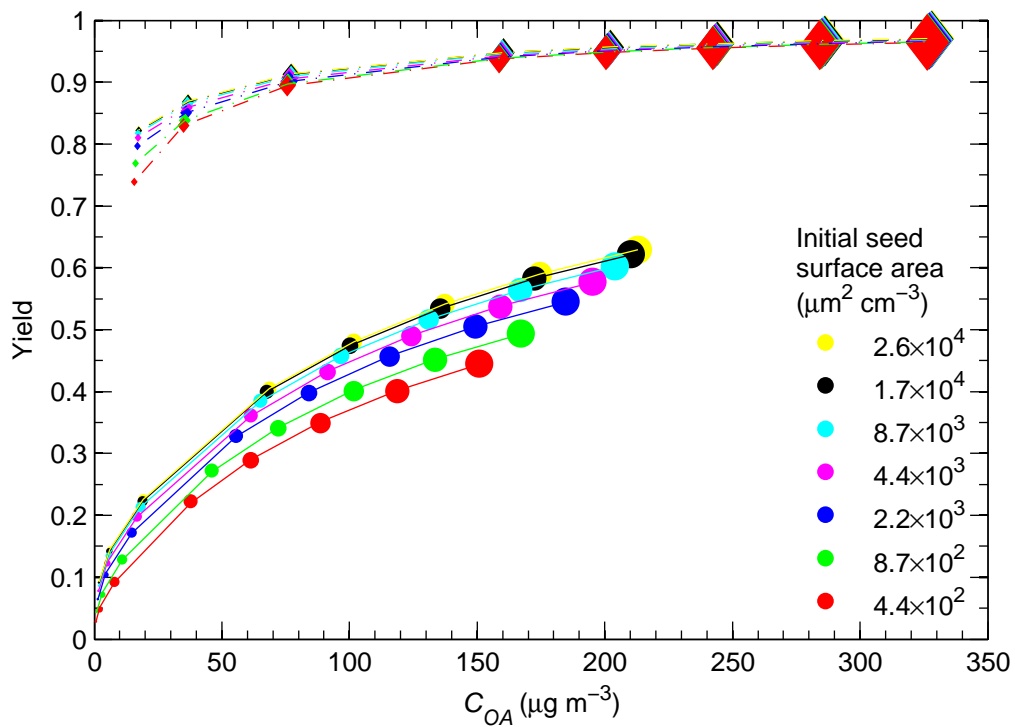
Figure S1: SOA yields after 20 h of simulation as a function of the final organic aerosol concentration C_{OA} for $\alpha_p = 0.01$. The points on the curve were generated by varying the initial parent VOC concentration G_{A0} with (circles) and without (diamonds) vapor wall deposition. The size of the markers increases as G_{A0} increases and colors correspond to different values of the initial seed surface area. The lines were generated by fitting a two-product model to the datapoints.
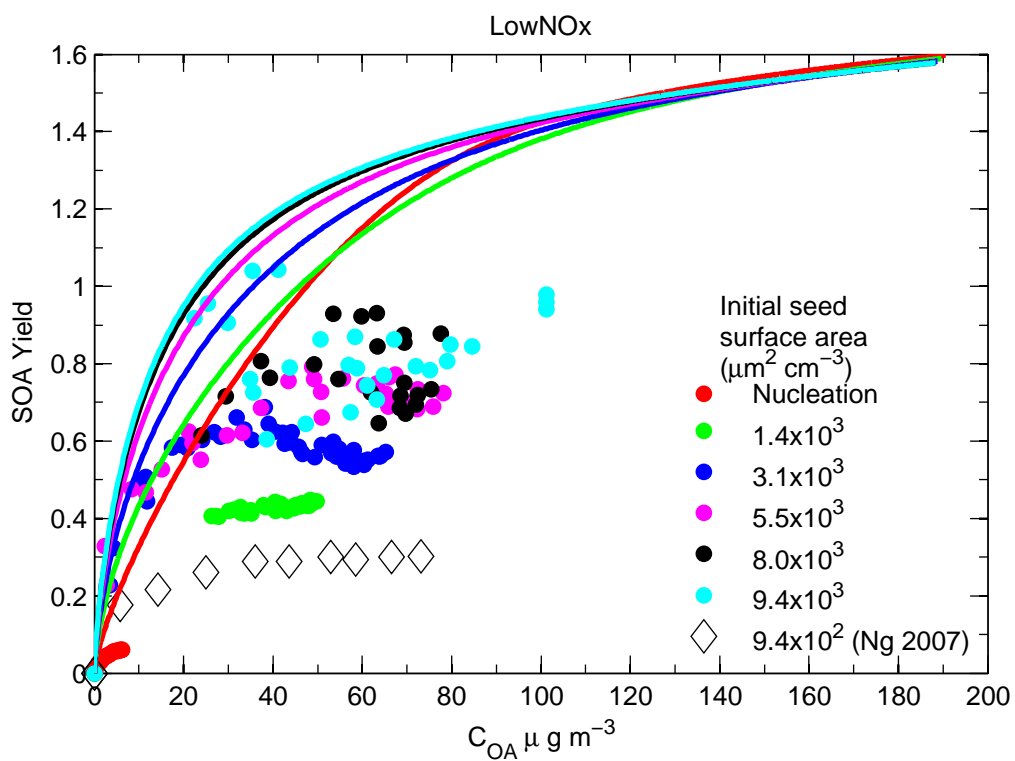
Figure S2: SOA yields over the course of each toluene low-NO$_x$ photooxidation experiment in (*11*) as a function of C_{OA} for different seed surface areas are shown as circles. Lines are yields calculated using the SOM model with wall deposition turned off (see *SI* of (*11*) for more details). Yields over the course of one representative experiment from (*33*) are shown as diamonds for comparison.
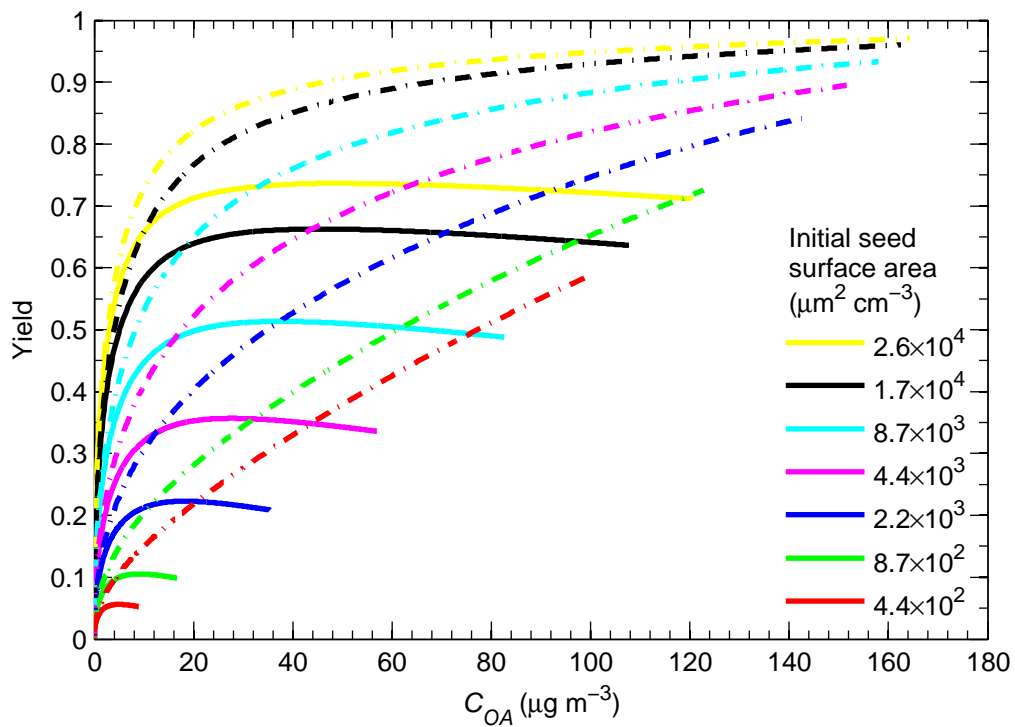
Figure S3: SOA yields are shown as a function of C_{OA} over the course of a simulation using the present model, with $C_{B-D}^* = 10^{-3}$ μ g m^{-3} and $\alpha_p = 0.001$. Yields are calculated in the presence (solid lines) and absence (dashed lines) of vapor wall deposition. Different initial seed surface areas are shown using different colors.
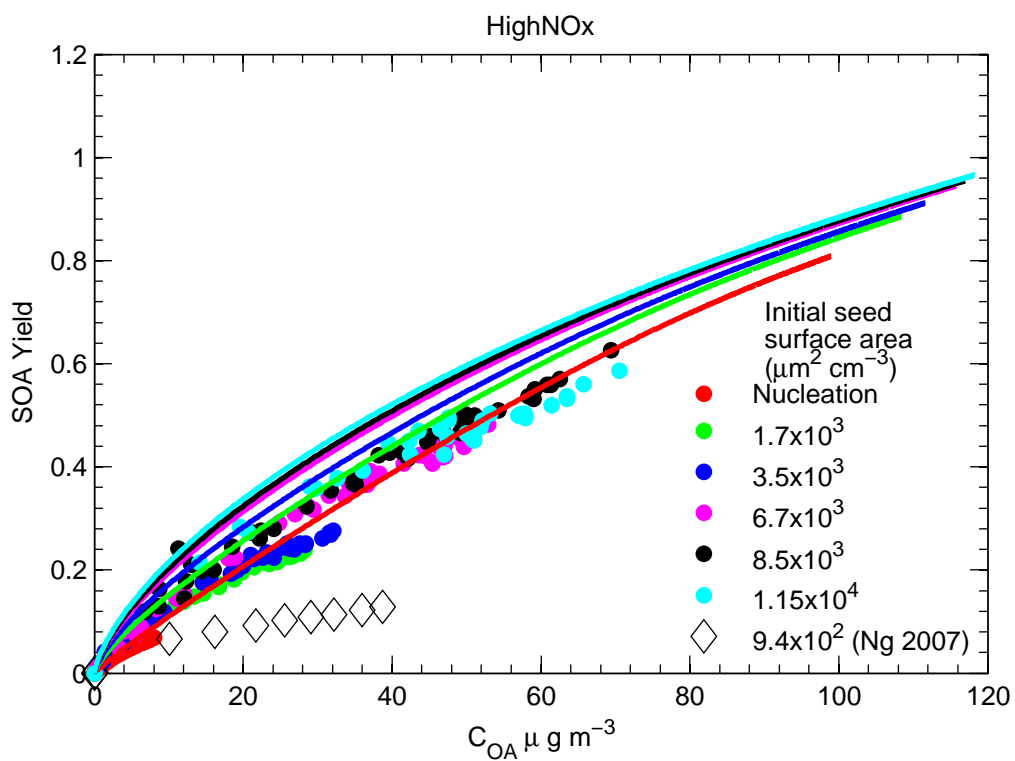
Figure S4: SOA yields over the course of each toluene high-NO$_x$ photooxidation experiment in (*11*) a function of C_{OA} for different seed surface areas are shown as circles. Lines are yields calculated using the SOM model with wall deposition turned off (see *SI* of (*11*) for more details). Yields over the course of one representative experiment from (*33*) are shown as diamonds for comparison.
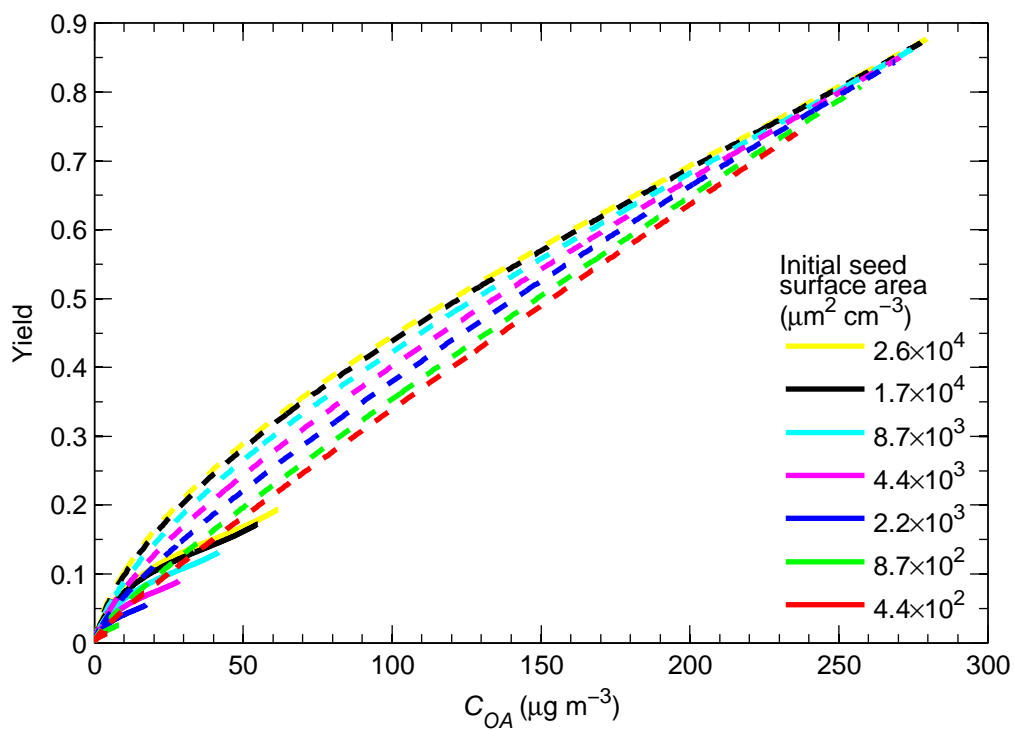
Figure S5: SOA yields are shown as a function of C_{OA} over the course of a simulation using the present model, with $C_i^* = [10^3 \ 10^1 \ 10^{-1}] \ \mu g \ m^{-3}$, $k[OH]_{A \to B} = k[OH]_{B \to C} = 5 \times 10^{-5} \ s^{-1}$ and $k[OH]_{C \to D} = 5 \times 10^{-4} \ s^{-1}$, and $\alpha_p = 0.001$. Yields are calculated in the presence (solid lines) and absence (dashed lines) of vapor wall deposition. Different initial seed surface areas are shown using different colors.
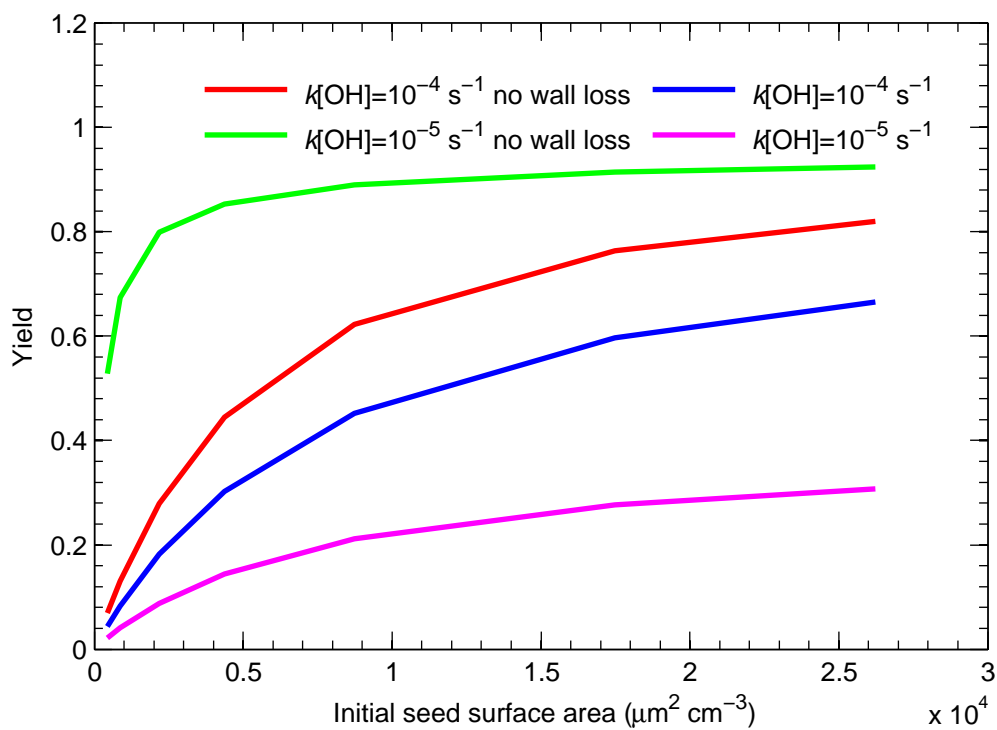
Figure S6: SOA yields after an equivalent amount of OH exposure (20 h for $k[\mathrm{OH}]_{A \to B} = 10^{-5}\ \mathrm{s}^{-1}$ and 2 h for $k[\mathrm{OH}]_{A \to B} = 10^{-4}\ \mathrm{s}^{-1}$) as a function of the final organic aerosol concentration C_{OA} for simulations with $\alpha_p = 0.001$ for different values of $k[\mathrm{OH}]_{A \to B}$, with and without vapor wall deposition.
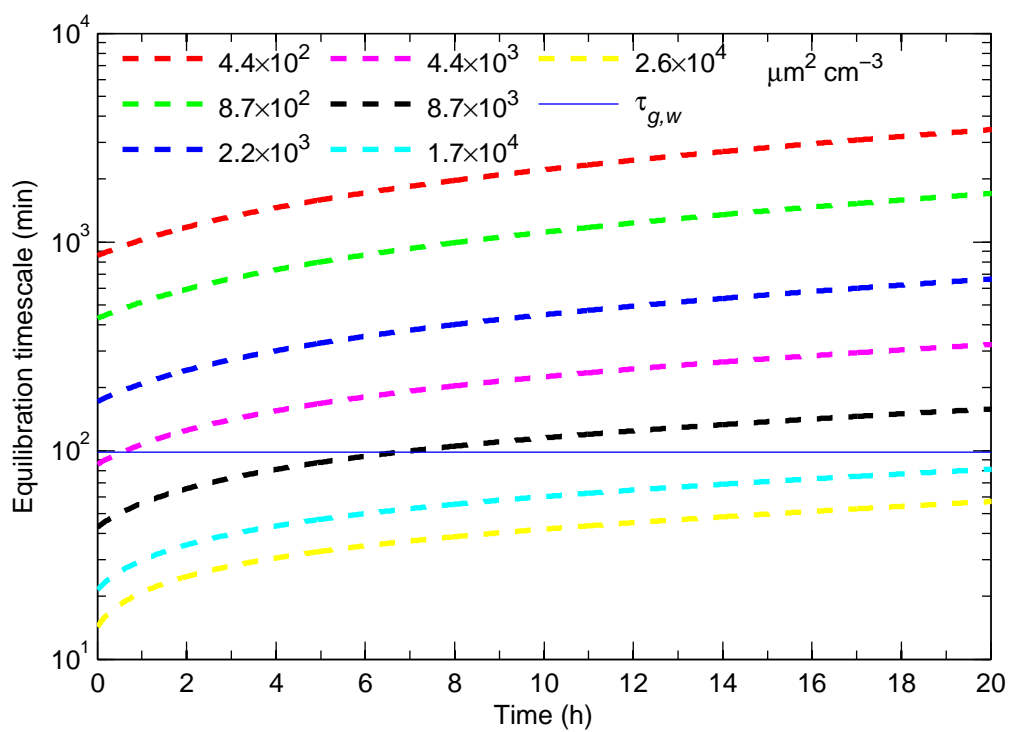
Figure S7: Time evolution of equilibration timescale for gas-particle partitioning $\tau_{g,p}$ for different initial seed surface areas. The equilibration timescale for gas-wall partitioning ($\tau_{g,w} = 1/k_{wall,on}$) is shown as a horizontal line because this timescale does not change with time.